J. Fluid Mech. (2007), *vol.* 590, *pp.* 471–496.
doi:10.1017/S0022112007008105 Printed in the United Kingdom

Stability control and catastrophic transition in a forced Taylor–Couette system

M. AVILA[1], F. MARQUES[1], J. M. LOPEZ[2] AND A. MESEGUER[1]

[1]Departament de Física Aplicada, Univ. Politècnica de Catalunya, Barcelona 08034, Spain

[2]Department of Mathematics and Statistics, Arizona State University, Tempe, AZ 85287, USA

(Received 25 January 2007 and in revised form 4 July 2007)

Harmonic axial motion of the inner cylinder in the Taylor–Couette system can efficiently shift the onset of instability to larger inner cylinder rotation rates. However, once instability has set in, a rapid sequence of symmetry-breaking bifurcations results in complex spatio-temporal dynamics even for very low post-critical values of the rotation rate. Using spectral computations, we present a detailed study of this sudden transition, shedding light on the nature of the complex flows observed in recent laboratory experiments. In particular, it is shown that these bifurcations are responsible for some of the experimentally observed frequencies which had been attributed to background noise. Movies are available with the online version of the paper.

1. Introduction

The flow of a viscous fluid contained in the gap between two rotating cylinders, known as Taylor–Couette flow, has been a paradigm for the study of the transition from a simple laminar flow, circular Couette flow, to turbulence following a progression of instabilities to flow states with increasing spatial and temporal complexity (Coles 1965; Andereck, Liu & Swinney 1986). Tagg (1994) provides a guide to the extensive literature on this problem. When the outer cylinder is at rest, the first bifurcation results in Taylor vortex flow (TVF), a steady axisymmetric state consisting of pairs of counter-rotating meridional vortices, periodic in the axial direction.

Several variations of the Taylor–Couette problem have focused on the degree of stabilization that can be achieved, i.e. on the degree to which the threshold for the onset of Taylor vortex flow can be shifted to larger Reynolds numbers (a non-dimensional measure of the rotation of the inner cylinder). For example, the superposition of an axial pressure-driven through-flow has been shown to be an efficient mechanism to stabilize the basic flow (Snyder 1962; Takeuchi & Jankowski 1981; Meseguer & Marques 2002). The effects on the nonlinear dynamics are complex and have been studied experimentally (Lueptow, Docter & Min 1992; Tsameret & Steinberg 1994; Wereley & Lueptow 1999).

Axial sliding of the inner cylinder has also been investigated as a stabilization strategy, beginning with the pioneering experimental and analytical work of Ludwieg (1964). However, much less attention has been paid to this problem, mainly due to the technical difficulties in its experimental realization. This problem can be formulated either as an open flow system or an enclosed system with endwalls. Ali & Weidman (1993) studied the stability of the latter, and more recently Meseguer & Marques (2000) compared the two systems. They focused on the former and showed that

stability is enhanced only for slow axial sliding, but that the difference between systems is small.

Hu & Kelly (1995) considered temporal modulations of both Poiseuille flow and axial sliding in the open Taylor–Couette system. They performed a Floquet analysis of the resulting periodic basic states and showed that both mechanisms are more efficient in delaying transition than the corresponding steady flows. Their results motivated the experimental work of Weisberg, Kevrekidis & Smits (1997) to verify this effect and devise transition control mechanisms based on axial oscillations of the inner cylinder. However, there was only qualitative agreement between the experiments and the numerical Floquet analysis. Marques & Lopez (1997) showed that the discrepancy was due to the presence of endwalls in the experiment, in contrast to the open flow system considered by Hu & Kelly (1995). The Floquet analysis by Marques & Lopez (1997) accounted for the leading-order effects of the presence of endwalls by imposing a zero axial mass flow, and despite the fact that their model retained the idealization of infinitely long cylinders, the agreement with the experiments was excellent.

Although the transition to TVF when the inner cylinder is forced to oscillate harmonically in the axial direction is generally via a synchronous bifurcation to axisymmetric cells, Marques & Lopez (1997) noted that for small frequencies and large amplitudes of the axial oscillations there are some windows of parameter space where the transition is via a Neimark–Sacker bifurcation (a Hopf bifurcation from a periodic orbit) to non-axisymmetric spiral flow. In this case, the time-periodic basic state bifurcates to a quasi-periodic torus featuring the forcing frequency, ω_f, and the frequency of the spiral mode, ω_s. These windows of parameter space were investigated by Marques & Lopez (2000) using Floquet analysis to identify the presence of several strong resonances, i.e. $\omega_s/\omega_f = p/q$ with $q \leqslant 4$. That linear analysis motivated the recent experiments by Sinha, Kevrekidis & Smits (2006) who investigated the associated nonlinear dynamics and identified regions of quasi-periodic motion and frequency-locking, as well as observing the torus to break up for higher post-critical values of the Reynolds number. However, the results they obtained were noisy even for Reynolds numbers very close to critical. The signals they analysed contained additional frequencies which were not a linear combination of ω_f and ω_s, and were attributed to background noise.

In order to shed light on the transition to complex behaviour in periodically forced systems and clarify the results of Sinha *et al.* (2006), we have numerically solved the unsteady Navier–Stokes equations with highly accurate spectral computations. We have found that subsequent bifurcations occurring very close to onset of the first instability of the basic state, which are not detectable in the experiments due to the precision that can be achieved, destroy the torus and introduce additional independent frequencies into the solutions. Moreover, our theoretical analysis shows that due to the symmetries of the system under consideration, frequency-locking is not possible until the bifurcating flow has broken the translational and rotational symmetries. As this happens through the introduction of new independent frequencies, any observed frequency-locking must be only partial and therefore does not involve periodic flow.

The paper is structured as follows. The formulation and symmetries of the problem are discussed in § 2, where the numerical discretization employed in order to detect the bifurcations occurring in the axially forced case is presented. Section 3 deals with the transition to complex dynamics, giving a detailed account of the progression of flows leading to the complex flow observed in the experiments of Sinha *et al.* (2006). In § 4 the presence of partial frequency-locking for non-symmetric flows is discussed, whereas in Appendix A it is shown from normal-form analysis that resonances are

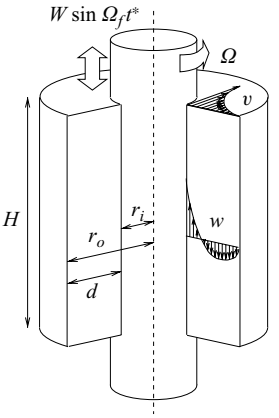

FIGURE 1. Schematic of Taylor–Couette flow with axial oscillations of the inner cylinder.

inhibited due to the symmetries of the system, so that at onset of instability the nonlinear dynamics in a neighbourhood of the Neimark–Sacker bifurcation can be unfolded with a single parameter.

2. Numerical formulation and symmetries

Consider an incompressible fluid of kinematic viscosity ν and density ϱ which is contained between two concentric cylinders whose inner and outer radii are r_i and r_o. The outer cylinder is stationary and the inner cylinder rotates at a constant angular velocity Ω while executing harmonic oscillations in the axial direction with velocity $W \sin \Omega_f t^*$.

Figure 1 shows a schematic of the flow. The independent dimensionless parameters in this problem are: the radius ratio $\eta = r_i/r_o$, which fixes the geometry of the annulus; the Couette flow Reynolds number $Re = \Omega d r_i/\nu$, where $d = r_o - r_i$; and the non-dimensional amplitude $\mathscr{A} = Wd/\nu$ and frequency $\omega_f = \Omega_f d^2/\nu$ of the forcing. The experimental apparatus of Sinha *et al.* (2006) had a radius ratio of $\eta = 0.905$, and we have used the same value in our computations. Moreover, in the experiment the amplitude and frequency of the axial motion were mechanically coupled such that $\omega_f = \mathscr{A}/9.525$; we have used this relationship in our computations presented here.

Space and time are scaled by d and d^2/ν, respectively. The Navier–Stokes equations and the incompressibility condition for this scaling are

$$\partial_t \boldsymbol{v} + (\boldsymbol{v}\cdot\nabla)\boldsymbol{v} = -\nabla p + \Delta \boldsymbol{v}, \quad \nabla\cdot\boldsymbol{v} = 0. \tag{2.1}$$

The boundary conditions in cylindrical coordinates are

$$\boldsymbol{v}(r_i, \theta, z, t) = (0, Re, \mathscr{A}\sin\omega_f t), \quad \boldsymbol{v}(r_o, \theta, z, t) = \boldsymbol{0}. \tag{2.2}$$

In the experiments of Sinha *et al.* (2006), the aspect ratio of the annulus is very large, $H/d = 152$. We assume periodicity in the axial direction, with fundamental axial wavenumber k_0 and corresponding wavelength $\Lambda = 2\pi/k_0$. Moreover, we account for the leading-order effects of the presence of endwalls by imposing a zero net axial mass flow at every instant in time (*enclosed flow* condition). The resulting basic flow is ($T_f = 2\pi/\omega_f$)-periodic and consists of the superposition of the circular Couette flow

and the axial annular Stokes flow

$$\boldsymbol{v}_b = \left(0, \frac{\eta Re}{1-\eta^2}\left(\frac{r_o}{r} - \frac{r}{r_o}\right), \mathscr{A} f(r)\sin(\omega_f t + \alpha(r))\right), \tag{2.3}$$

where $g(r) = f(r)\mathrm{e}^{\mathrm{i}\alpha(r)}$ is the solution of a second-order ODE satisfying the boundary conditions of the problem and the enclosed flow condition:

$$g'' + \frac{1}{r}g' - \mathrm{i}\omega g = p_0, \quad g(r_i) = 1, \quad g(r_o) = 0, \quad \int_{r_i}^{r_o} r g(r)\mathrm{d}r = 0. \tag{2.4}$$

The constant p_0 is related to the axial pressure gradient needed to enforce the enclosed flow condition. An explicit solution involving modified Bessel functions is given in Marques & Lopez (1997), along with asymptotic expansions and other properties of g, but it is more practical to numerically compute g by solving (2.4) with efficient spectral methods. Here, we have used collocation at Gauss–Lobatto points.

The basic flow (2.3) can be used to simplify the numerical scheme by decomposing the velocity field and pressure as

$$\boldsymbol{v}(r,\theta,z,t) = \boldsymbol{v}_b(r,t) + \boldsymbol{u}(r,\theta,z,t), \tag{2.5}$$

$$\boldsymbol{\nabla}\cdot\boldsymbol{u} = 0, \ \ \boldsymbol{u}(r=r_i) = \boldsymbol{u}(r=r_o) = \boldsymbol{0}, \tag{2.6}$$

$$p(r,\theta,z,t) = p_b(z) + q(r,\theta,z,t), \tag{2.7}$$

where $\boldsymbol{u}$ is a solenoidal velocity field vanishing at the cylinder walls and satisfying the enclosed flow condition. We discretize the perturbation $\boldsymbol{u}$ by a spectral approximation $\boldsymbol{u}_\mathrm{s}$ of order L in z, order N in θ, and order M in r,

$$\boldsymbol{u}_\mathrm{s}(r,\theta,z,t) = \sum_{l=-L}^{L}\sum_{n=-N}^{N}\sum_{m=0}^{M} a_{lnm}(t)\mathrm{e}^{\mathrm{i}(lk_0 z + n\theta)}\boldsymbol{v}_{lnm}(r). \tag{2.8}$$

Expansion (2.8) is introduced in (2.5) and the resulting expression for the velocity field $\boldsymbol{v}$ is substituted in (2.1). The spectral scheme is obtained by projecting (2.1) over a suitable set of test solenoidal fields, thus eliminating the pressure. This projection yields a system of ODEs for $a_{lnm}(t)$ which is integrated in time by a linearly implicit method, where backwards differences are used for the linear part and polynomial extrapolation is used for the nonlinear part. The details have been published in Avila, Meseguer & Marques (2006). The code has been tested in the linear and nonlinear regimes against the results of Meseguer & Marques (2002) and Jones (1985).

2.1. *Fundamentals of instability and transition*

Note that in the infinite-cylinder idealization, the spectrum of axial wavenumbers k is continuous. However, when the spectral approximation (2.8) is used in the nonlinear computations, the spectrum of axial wavenumbers becomes discrete. In the computations, a fundamental axial wavenumber k_0 is selected such that the discretization resolves the modes responsible for the instability, as well as their leading harmonics. A spectral resolution consisting of $(L, M, N) = (65, 16, 20)$ modes along with $k_0 = 0.196$, leading to a wavelength of $\Lambda \sim 32$ has been implemented here. The value of k_0 has been chosen in order to capture the dynamics arising in the neighbourhood of the resonant point $\mathscr{A} = 79.25$, $Re_c = 244.74$ (identified in the Floquet analysis). In particular, the $(l, n) = (12, \pm 1)$ Fourier modes in the expansion (2.8) have an axial wavenumber of $k = 12k_0 = 2.35$, which is very close to the critical axial wavenumber of the infinite case $k_c = 2.36$. Overall, with $L = 65$ our nonlinear computations include up to four harmonics of the most dangerous modes

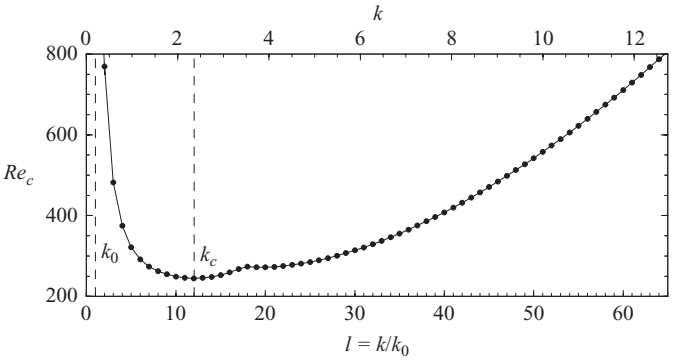

FIGURE 2. Neutral stability curve of the azimuthal modes $n = \pm 1$ for $\mathscr{A} = 79.25$ as computed with Floquet analysis. The circles are the discrete set of axial wavenumbers corresponding to the Fourier modes used in the nonlinear computations (2.8). The first Fourier mode $(l, n) = (1, 1)$, with smallest axial wavenumber $k = k_0 = 0.196$, is not shown as the corresponding $Re_c = 16\,256$ is off the scale of the plot. The most unstable mode is $(l, n) = (12, 1)$, with axial wavenumber $k = 12k_0 = 2.35$, which is very close to the critical axial wavenumber of the infinite case $k_c = 2.36$.

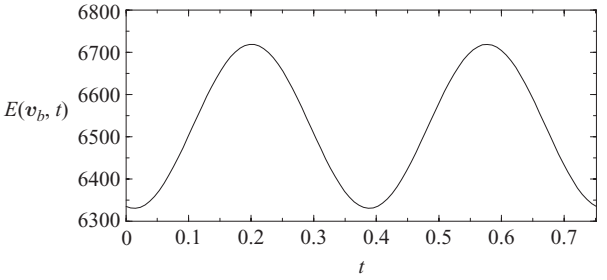

FIGURE 3. Kinetic energy time series of basic flow (2.3) over a forcing period. The parameter values are $Re = 200$, $\mathscr{A} = 79.6$.

$(l = 11, 12, 13)$. Figure 2 shows the neutral stability curve of the azimuthal modes $n = \pm 1$ for $\mathscr{A} = 79.25$, found using Floquet analysis. The discrete axial wavenumbers considered in the nonlinear computations are shown as filled circles on the curve.

Above the neutral stability curve of figure 2, the basic flow $\boldsymbol{v}_b$ becomes unstable. In the nonlinear computations, the instability is detected by monitoring the behaviour of the kinetic energy of the velocity field $\boldsymbol{v}$:

$$E(\boldsymbol{v}, t) = \frac{1}{2V} \int_0^H \mathrm{d}z \int_0^{2\pi} \mathrm{d}\theta \int_{r_i}^{r_o} \boldsymbol{v}^* \cdot \boldsymbol{v}\, r\, \mathrm{d}r, \tag{2.9}$$

where V is the volume of the annulus and * denotes complex conjugate. Figure 3 shows a kinetic energy time series of the basic flow, $\boldsymbol{v} = \boldsymbol{v}_b$, over a forcing period T_f. The time series is $T_f/2$-periodic, the two peaks corresponding to the forcing at maximum amplitude and opposite axial directions of the motion of the inner cylinder.

It is convenient to consider the kinetic energy of the perturbation field $\boldsymbol{u}$, $E(\boldsymbol{u}, t)$. Since the basic flow has $\boldsymbol{u} = 0$, a non-zero value of $E(\boldsymbol{u}, t)$ indicates that the basic state has become unstable and a new state has bifurcated. However, the kinetic energy of the perturbation field alone does not provide information on the dominant axial and azimuthal wavenumbers of the bifurcated solutions. In order to characterize the

spatial complexity of these flows, we consider the kinetic energy associated with each Fourier mode in the spectral approximation (2.8):

$$\mathrm{E}_{ln}(t) = \frac{1}{2V}\int_0^{\Lambda} \mathrm{d}z \int_0^{2\pi} \mathrm{d}\theta \int_{r_i}^{r_o} \boldsymbol{u}_{ln}^{*} \cdot \boldsymbol{u}_{ln}\, r\, \mathrm{d}r, \tag{2.10}$$

where $\boldsymbol{u}_{ln}$ is the (l, n) component of the perturbation field $\boldsymbol{u}$:

$$\boldsymbol{u}_{ln} = \mathrm{e}^{\mathrm{i}(lk_0 z + n\theta)} \sum_{m=0}^{M} a_{lnm}(t)\boldsymbol{v}_{lnm}(r). \tag{2.11}$$

Note that due to the mutual orthogonality of the Fourier modes, this decomposition yields

$$E(\boldsymbol{u}, t) = \sum_{l=-L}^{L} \sum_{n=-N}^{N} \mathrm{E}_{ln}(t). \tag{2.12}$$

The changes in the distribution of modal energies of the solutions as the Reynolds number is further increased aids in identifying subsequent bifurcations and in elucidating the increased complexity of the resulting flow patterns.

2.2. *Symmetries*

The governing equations and boundary conditions are invariant under rotations R_α about, and translations T_a along, the common axis of the cylinders. Rotations generate the symmetry group $SO(2)$, and due to the imposed axial periodicity of wavelength Λ, axial translations generate another $SO(2)$ symmetry group. As both actions commute, the group of spatial symmetries of the system is $\mathscr{G}_0 = SO(2) \times SO(2)$. There is an additional spatio-temporal symmetry S, which consists of a time translation of half a period, $\phi^{T/2}$, followed by a reflection about a plane orthogonal to the cylinder axis F_z (acting as $z \to -z$). The actions of these on the velocity are

$$R_\alpha(\boldsymbol{v})(r, \theta, z) = \boldsymbol{v}(r, \theta + \alpha, z), \tag{2.13}$$

$$T_a(\boldsymbol{v})(r, \theta, z) = \boldsymbol{v}(r, \theta, z + a), \tag{2.14}$$

$$F_z(\boldsymbol{v})(r, \theta, z) = (v_r, v_\theta, -v_z)(r, \theta, -z), \tag{2.15}$$

$$\phi^{T/2}(\boldsymbol{v})(r, \theta, z, t) = \boldsymbol{v}(r, \theta, z, t + T/2). \tag{2.16}$$

$S = F_z \circ \phi^{T/2}$ commutes with rotations but not with translations: $ST_a = T_{-a}S$. If S were purely spatial, i.e. the reflection F_z, then S and T_a would generate the orthogonal group, $O(2) = SO(2) \rtimes Z_2$ (semidirect product), where the elements of Z_2 would be F_z and the identity. As S is a space–time symmetry, S and T_a generate a space–time symmetry group isomorphic to $O(2)$, $O(2)_{ST} = SO(2) \rtimes Z_2$, where now the elements of Z_2 are S and the identity. The complete symmetry group of the problem is $\mathscr{G} = SO(2) \times O(2)_{ST}$. The basic flow (2.3) is invariant under $\mathscr{G}$.

It is important to note that in many studies of flows in long cylinders, a spatial periodicity of wavelength $\lambda_c = 2\pi/k_c$ in the axial direction is assumed (where k_c is the critical axial wavenumber obtained from linear stability analysis). This assumption, which corresponds to fixing $k_0 = k_c$ in (2.8), renders the $l = 1$ axial mode the only one unstable in the parameter regime of study and results in the computations being unable to investigate the competition between different spatial modes (except in the exceptional cases that their wavelengths are simple rational ratios). If this imposed axial periodicity is destroyed in subsequent bifurcations due to mode competition, as is the case in the present problem, a much larger axial periodicity $\Lambda = 2\pi/k_0$, with

$k_0 \ll k_c$, must be considered instead. The discretization of the problem is still periodic, so the wavenumber ratio between different competing modes is rational, but our discretization presented in § 2.1 allows for rational ratios with large denominators. The interaction of these modes is practically indistinguishable from truly quasi-periodic solutions.

3. Transition to complex spatio-temporal dynamics

The experiments of Weisberg *et al.* (1997) and the Floquet analysis of Marques & Lopez (1997) showed that the stability of Couette flow can be greatly enhanced by harmonic axial motion of the inner cylinder. Although this forcing stabilizes both axisymmetric and non-axisymmetric modes, there are windows in parameter space where the onset of instability is to spiral modes via a Neimark–Sacker bifurcation (a Hopf bifurcation from a periodic orbit). Marques & Lopez (2000) showed that in these windows strong resonances between the Neimark–Sacker frequency ω_s and the forcing frequency ω_f occur, motivating the recent experiments by Sinha *et al.* (2006) who studied the complex nonlinear dynamics subsequent to the Neimark–Sacker bifurcation. Nevertheless, their results contained additional frequencies which could not be identified and were attributed to background noise.

We show that these additional frequencies are due to subsequent bifurcations taking place very close to the first onset of instability. The increments in Re at which these additional bifurcations occur are so small (about 0.4%) that they cannot be detected with the precision that could be achieved in the experiments (the experimental uncertainty in Re was about 3%). A consequence of this rapid succession of bifurcations following the loss of stability of the temporally forced Couette flow is that the resulting state has much greater spatio-temporal complexity than the unforced state at the same Re (which is the wavy vortex flow). Therefore, there is a trade-off between the enhanced stability and the spatio-temporal complexity of the flows once instability has arisen. For the axial forcing amplitudes considered in the experiments and here ($\mathscr{A} \sim 80$), the critical Reynolds number Re_c for instability of Couette flow is about 80% higher than in the unforced case. Nevertheless, for the axially forced case the flow begins to lose regularity in axial and azimuthal wavenumber for Re about 2% above criticality due to the sequence of bifurcations.

3.1. *Onset of instability*

The spiral modes predicted by the Floquet analysis of Marques & Lopez (2000), from now on referred to as Mode 1 (M1), bifurcate supercritically from the oscillating basic state (2.3) in a Neimark–Sacker bifurcation. They are characterized by their axial and azimuthal wavenumbers (k, n) which define a constant spiral angle $\beta = \tan^{-1}(-n/k)$. In particular, the full nonlinear solution is of the form $\boldsymbol{f}(r, t, \omega_s t + kz + n\theta)$; $\boldsymbol{f}$ is T_f-periodic in the second argument and 2π-periodic in the third argument. Figure 4(a) shows a grey-scale snapshot of the azimuthal vorticity at the outer cylinder, in a (θ, z) planar rendering of the cylinder surface for M1 at $\mathscr{A} = 79.6$ and $Re = 246.32$. Note that the azimuthal vorticity is constant over straight lines of angle β. Figure 4(b) shows a grey-scale snapshot of the kinetic energy of the Fourier modes $\mathrm{E}_{ln}(t)$. The leading mode is $(l, n) = (12, 1)$, i.e. with axial wavenumber $k = 12k_0 = 2.35$, which renders a spiral angle of $\beta \sim -23^\circ$.

The translational and rotational symmetries of the basic flow are broken, but M1 retains a helical symmetry $H_\alpha = R_\alpha T_{-n\alpha/k}$, which consists of an arbitrary rotation R_α composed with an axial translation $T_{-n\alpha/k}$, leaving the phase $kz + n\theta$ invariant;

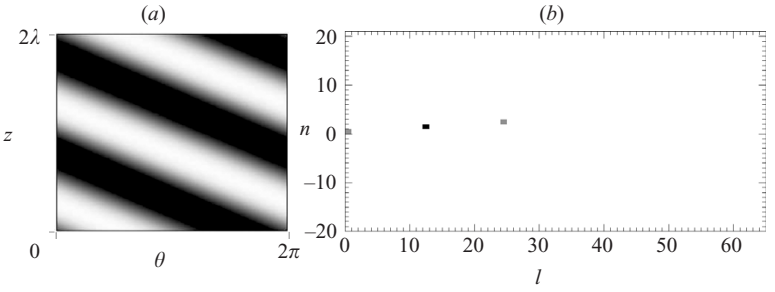

FIGURE 4. (*a*) Planar (θ, z) rendering of a grey-scale snapshot of the azimuthal vorticity of the perturbation $\boldsymbol{u}$ at the outer cylinder $r = r_o$, where black (white) corresponds to positive (negative) values. A (*b*) snapshot of the kinetic energies of the Fourier modes $E_{ln}(t)$ in a logarithmic grey-scale map black corresponds to the energy of the leading mode and white to a level seven orders of magnitude lower (Movie 1 with the online version shows their temporal evolution over two forcing periods). The flow is M1 at $\mathscr{A} = 79.6$ and $Re = 246.32$.

the bifurcated solution is a spiral wave that is modulated by the harmonic forcing. However, due to the helical symmetry, strobing the solution at the forcing frequency renders the second argument in $\boldsymbol{f}$ constant and the strobed spiral pattern then precesses in the azimuthal direction with precession frequency $-\omega_s/n$. This azimuthal rotation can also be interpreted as an axial translation (barber-pole effect), with axial velocity $-\omega_s/k$. Therefore, M1 is a *relative periodic orbit*, in exactly the same way as rotating and travelling waves are *relative equilibria* (Rand 1982; Wulff, Lamb & Melbourne 2001). Movie 1 with the online version of the paper shows the temporal evolution of the corresponding snapshots in figure 4, where the barber-pole effect associated with ω_s and the modulation associated with ω_f are evident.

For the M1 case shown in figure 4, its radial velocity time series at the point $(r, \theta, z) = ((r_i + r_o)/2, 0, 0)$ along with the time series of its kinetic energy and the corresponding power spectra are shown in figure 5. The velocity time series and corresponding spectra indicate that M1 is quasi-periodic. However, as M1 is a relative periodic orbit, its kinetic energy has the form $g(r, t, \omega_s t + kz + n\theta)$ and is not modified by the presence of the spiral frequency ω_s. On integrating g over the whole domain, the $\omega_s t$ term is just a phase shift of the third argument; on integrating over a complete period, the shift does not modify the result and the dependence on $\omega_s t$ disappears, leaving only the T_f-periodic time dependence of the second argument (the periodic forcing), as shown in figures 5(*c*) and 5(*d*).

The Neimark–Sacker bifurcation also breaks the spatio-temporal symmetry S, resulting in two different M1, corresponding to left-handed ($n = 1$) and right-handed ($n = -1$) spirals related by the action of S. The right-handed spirals propagate in the negative axial direction whereas the left-handed spirals propagate in the positive axial direction. Figure 6 shows a grey-scale snapshot of the azimuthal vorticity at the outer cylinder (as would be seen by an observer situated opposite the apparatus; note that due to the parallel projection used in this rendering, distances are not preserved and the angle of the spirals appears distorted towards the sides of the image) of (*a*) left-handed and (*b*) right-handed M1 at $\mathscr{A} = 79.6$ and $Re = 246.32$ (onset of instability is at $Re_c = 245.42$); their temporal behaviour is shown in Movie 2 with the online version of the paper. Since the imposed periodic Stokes flow reverses its direction after half a forcing period, these solutions spend half the time travelling with and the other half travelling against the imposed flow. This behaviour is manifested in the kinetic

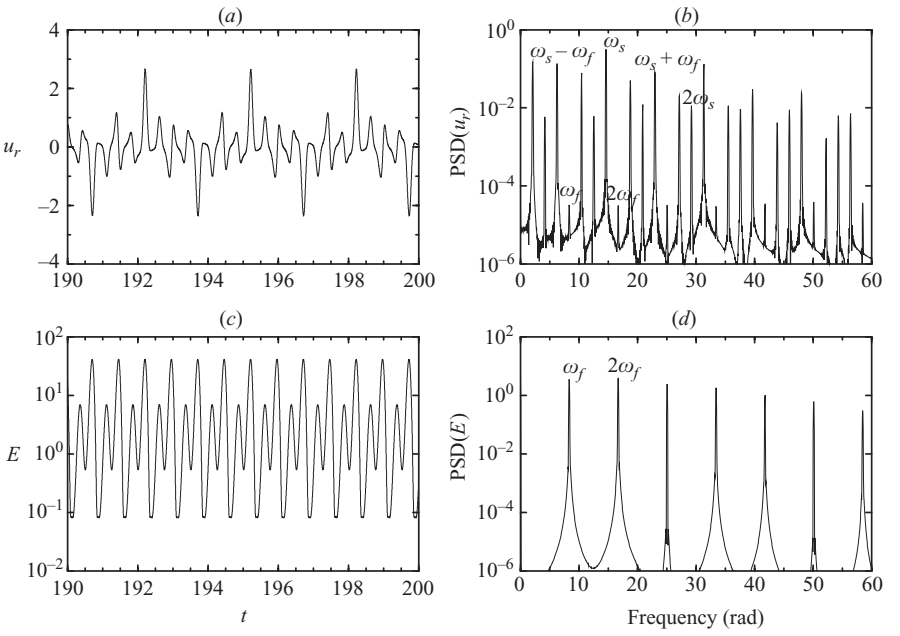

FIGURE 5. Time series of the radial velocity u_r at $(r, \theta, z) = ((r_i + r_o)/2, 0, 0)$ and the kinetic energy $E(\boldsymbol{u}, t)$, together with the corresponding power spectra, for the spiral waves (M1) shown in figure 6.

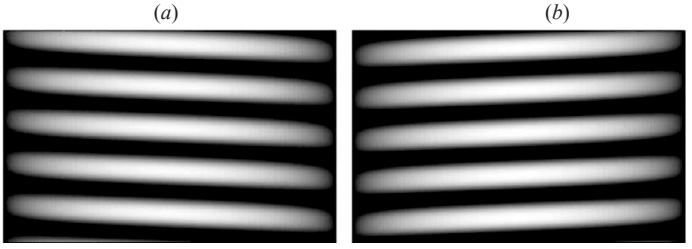

FIGURE 6. Perspective view (parallel projection of the cylinder). The grey-scale snapshot shows the intensity of azimuthal vorticity of the perturbation $\boldsymbol{u}$ at $r = r_o$. The flows are: (*a*) a left-handed upward propagating M1 and (*b*) a right-handed downward propagating M1, both at $\mathscr{A} = 79.6$ and $Re = 246.32$. Movie 2 with the online version of the paper illustrates their temporal behaviour.

energy time series of figure 5(*c*), which shows two peaks of different intensity at t and $t + T_f/2$ corresponding to propagation with (higher peak) and against (lower peak) the imposed Stokes flow, indicating that the S symmetry is broken by the bifurcation to M1. Note that for the S-symmetric basic flow the two peaks are identical (see figure 3). Therefore, the symmetry group of M1 is purely spatial, and its elements are the aforementioned helical motions H_α, generating a group isomorphic to $SO(2)$.

3.2. *Secondary bifurcations*

The M1 spiral waves that bifurcate from the basic flow are only stable in a very small region of parameter space, becoming unstable to a wavy spiral mode, M2. In particular, this secondary bifurcation occurs precisely at $\epsilon = (Re - Re_c)/Re_c = 0.0039$

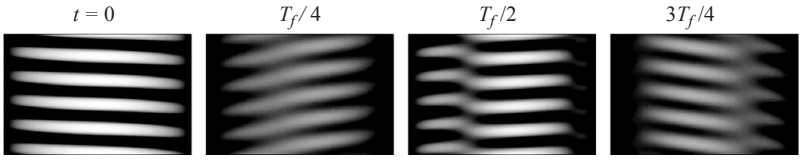

FIGURE 7. Snapshots of a perspective view (parallel projection of the cylinder). The grey-scale map shows the intensity of azimuthal vorticity of the perturbation $\boldsymbol{u}$ at $r = r_o$, where black (white) corresponds to positive (negative) values. The flow corresponds to M2 at $\mathscr{A} = 79.6$ and $Re = 247$ at 4 phases over one forcing period (Movie 3 with the online version of the paper shows the temporal behaviour over two forcing periods).

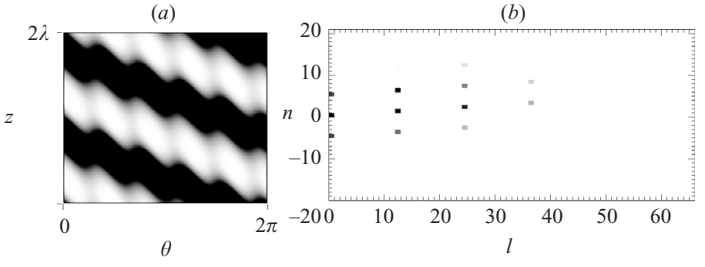

FIGURE 8. A figure 4 but for M2 at $\mathscr{A} = 79.6$ and $Re = 247$ (Movie 4 with the online version of the paper shows the temporal behaviour over two forcing periods).

which is an order of magnitude smaller than the experimental uncertainty in Re. Therefore, the M1 spiral waves born at onset are not observable in the experiments of Sinha *et al.* (2006). The M2 state is characterized by the axial and azimuthal wavenumbers (k, n) of the underlying spiral wave (M1), and the wavy azimuthal wavenumber n_w, which is typically $3 \leqslant |n_w| \leqslant 5$ depending on the parameter values and the initial conditions. In contrast to the constant spiral angle β characteristic of M1, the M2 wavy spirals have a time-dependent inclination, as illustrated in the flow snapshots in figure 7. Movie 3 with the online version of the paper shows the temporal behaviour of M2, and should be compared to Movie 2, corresponding to M1.

The bifurcation leading to M2 is not synchronous with the imposed Stokes flow, so that the wavy spirals have a new independent frequency ω_w which corresponds to a secondary Hopf bifurcation from the quasi-periodic M1 to the three-torus state M2. Nevertheless, as the spiral wave M1 is a relative periodic orbit with symmetry group $SO(2)$, the bifurcation to M2 is effectively a Neimark–Sacker bifurcation with $SO(2)$ symmetry (Wulff *et al.* 2001). The breaking of this symmetry results in a wavy flow with a discrete helical symmetry, as evident in figure 8(a). Instead of the straight lines of M1 in figure 4(a), the lines are modulated by the wavy azimuthal wavenumber $n_w = 5$. This can also be seen in the kinetic energies of the Fourier modes shown in the grey-scale snapshot in figure 8(b). M2 features an axial wavenumber of $k = 12k_0 = 2.35$ and an azimuthal wavenumber of $n = \pm 1$. Moreover, an additional mode $(0, n_w) = (0, 5)$ appears, along with all the linear combinations between (k, n) and $(0, n_w)$. Movie 4 with the online version of the paper shows the temporal behaviour of the spiral angle and the modal kinetic energies, $\mathrm{E}_{ln}(t)$, where the differences between M1 and M2 are evident when comparing with Movie 1. Therefore, the (θ, z)-dependence of M2 is of the form $\boldsymbol{f}(r, t, \omega_s t + kz + n\theta, \omega_w t + n_w\theta)$, where ω_w is the precession frequency associated to the wavy motion along the spiral pattern. The symmetry group of M2 is the discrete subgroup of $SO(2)$ generated by the helical symmetry $H_{\lambda/n_w} = R_{2\pi/n_w} T_{\lambda/n_w}$

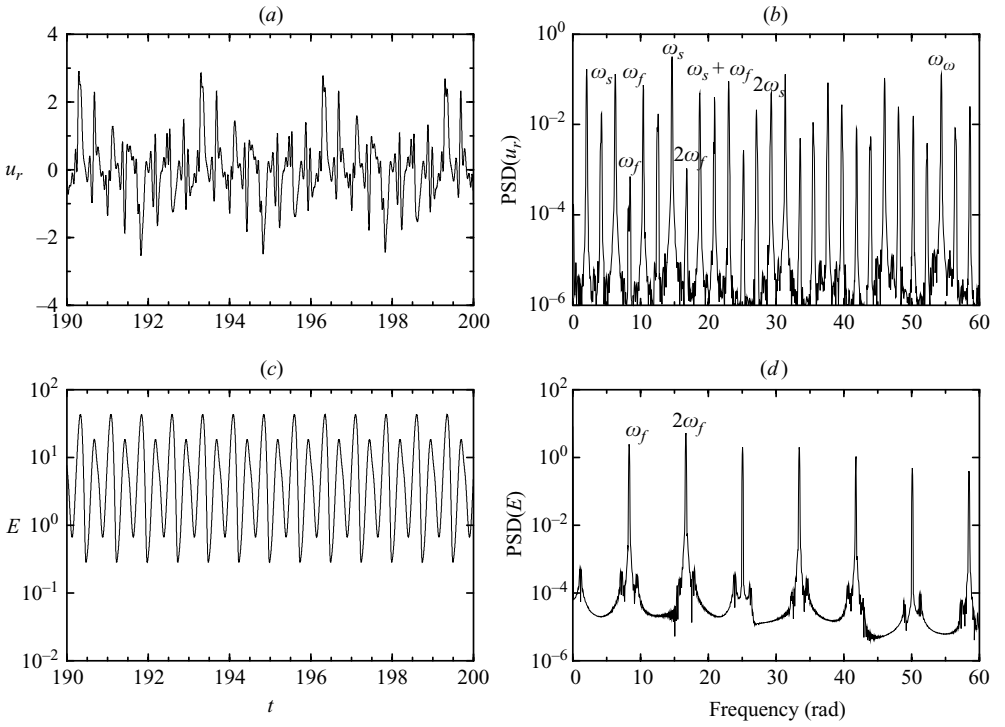

FIGURE 9. Time series of the radial velocity u_r at $(r, \theta, z) = ((r_i + r_o)/2, 0, 0)$, and the kinetic energy E, together with the corresponding power spectra, for the M2 wavy spirals shown in figures 7 and 8.

and their integer multiples, leaving both phases in $\boldsymbol{f}$ invariant; $\lambda = 2\pi/k$ is the axial wavelength of the spiral pattern. Due to the periodicity of the boundary conditions, this group is isomorphic to $\mathbb{Z}_{ln_w}$.

Figure 9 shows the time series of the radial velocity and kinetic energy, as well as the corresponding power spectra, of M2 at the same parameter values as in figures 7 and 8. In contrast to M1 in figure 5, an additional high-frequency modulation ω_w is evident in the radial velocity. Since ω_w is only associated with the precession speed of the wavy mode, it is not present in the kinetic energy time series, which has the form $g(r, t, \omega_s t + kz + n\theta, \omega_w t + n_w\theta)$. The base state has two periodic directions θ and z, and the two Hopf bifurcations correspond to time-dependent shifts in these directions. Integrating with respect to θ and z, the two frequencies ω_s and ω_w disappear, and the kinetic energy is simply T_f-periodic. In fact, in an appropriate rotating and axially translating reference frame, M2 is purely periodic and synchronous with the forcing. Although in the laboratory M2 has three independent frequencies and therefore resides on a three-torus, the two frequencies ω_s and ω_w are of a kinematic nature, so that the M2 wavy spirals are also relative periodic orbits.

M2 becomes unstable at a third bifurcation at $\epsilon = (Re - Re_c)/Re_c = 0.011$, evolving to a secondary wavy spiral state, termed M3. The visual differences between the wavy spirals M2 before and M3 after this bifurcation are difficult to discern in the laboratory frame (snapshots of M3 are shown in figure 10, and should be compared with the corresponding snapshots of M2 in figure 7; their temporal behaviours are shown in Movies 5 and 3 available with the online version). However, the (θ, z)-planar

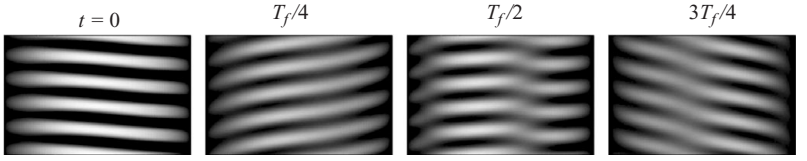

FIGURE 10. A figure 7 but the flow corresponds to M3 at $\mathscr{A} = 79.6$ and $Re = 249$. (Temporal behaviour is shown in Movie 5 with the online version of the paper).

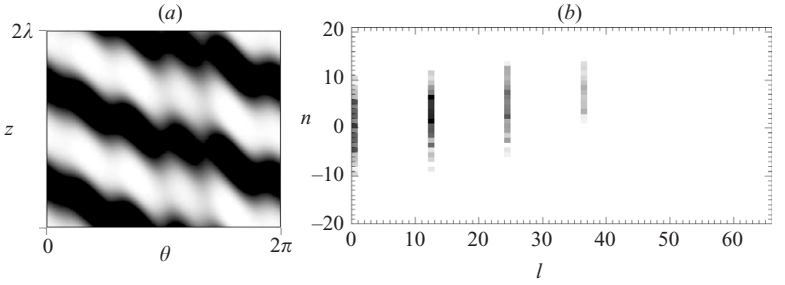

FIGURE 11. A figure 4 but for M3 at $\mathscr{A} = 79.6$ and $Re = 249$ (Movie 6 with the online version of the paper shows the temporal behaviour).

rendering of the cylinder surface in figure 11(a) reveals that the azimuthal periodicity of M2 has been lost, and M3 has defects in the azimuthal wavenumber. In particular, the kinetic energy of the Fourier modes shown in the grey-scale map of figure 11(b) elucidates that the spectrum in azimuthal wavenumbers is now full due to competition between different wavy modes. Therefore, the helical motion (H_{λ/n_w} generating $\mathbb{Z}_{ln_w}$) is no longer a symmetry of the pattern. Nevertheless, M3 still preserves the axial periodicity given by the axial wavenumber $k = 12k_0 = 2.35$, so that the subgroup of $\mathbb{Z}_{ln_w}$ generated by T_λ remains. This symmetry group contains only axial translations of a multiple of the axial wavelength of the pattern and it is isomorphic to $\mathbb{Z}_l$.

The time series and corresponding power spectra of the radial velocity and kinetic energy just beyond this third bifurcation at $\mathscr{A} = 79.6$ and $Re = 248.5$ are shown in figure 12. The characteristics of the radial velocity are very similar to those before the bifurcation (compare with figure 9), although the irregularities in azimuthal wavenumber result in a higher degree of irregularity in the signal. Moreover, the kinetic energy is no longer T_f-periodic. It is now quasi-periodic, modulated by the spiral frequency ω_s.

A very small further increase in Re results in the loss of the axial periodicity present in M3 (i.e. the remaining translational symmetry $\mathbb{Z}_l$ is broken). As a result of competition between different axial modes, a non-constant axial wavelength is evident in figure 13(a), showing a grey-scale snapshot of the azimuthal vorticity at the outer cylinder in a (z, θ)-planar rendering of the cylinder surface over the whole axial domain. At this bifurcation, the defective wavy spiral states, termed M4, emerge. These are characterized by a broad band in k. Figure 13(b) shows a snapshot of the kinetic energy of the Fourier modes for M4. The spectrum is full in both axial and azimuthal wavenumbers, illustrating the spatial complexity of this non-symmetric flow. Movie 7 shows the temporal behaviour of the snapshots in figure 13 over four forcing periods. The increased temporal complexity of M4 is clear in the radial velocity and kinetic energy time series and corresponding power spectra shown in figure 14. The defects in the axial and azimuthal wavenumbers lead to broad bands in both the spatial and temporal spectra.

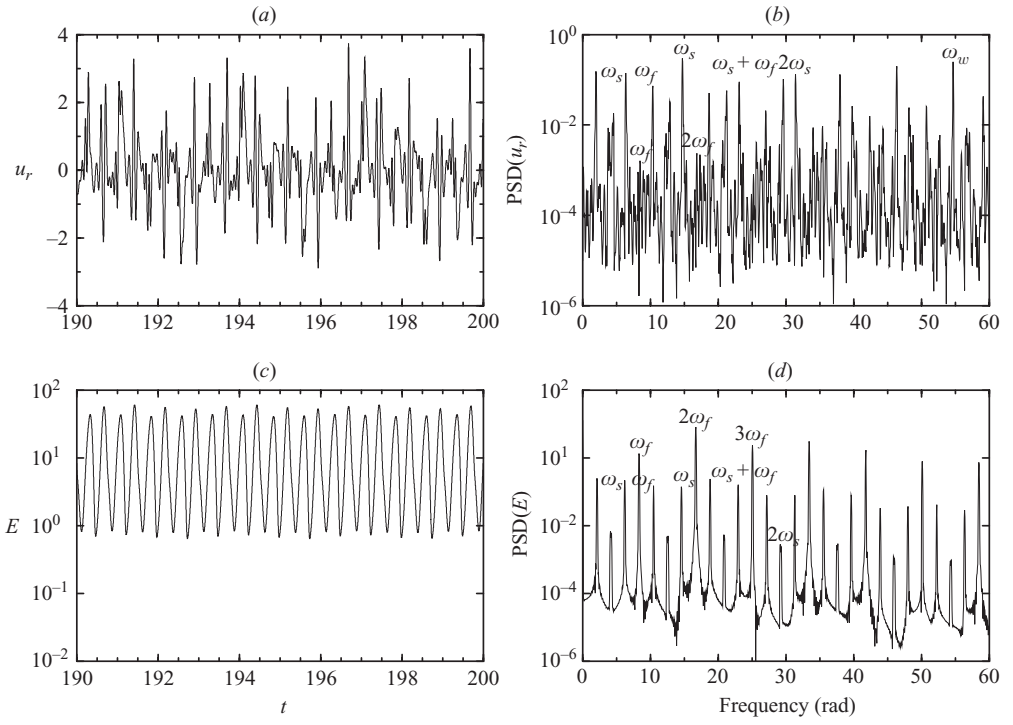

FIGURE 12. Time series of the radial velocity u_r at $(r, \theta, z) = ((r_i + r_o)/2, 0, 0)$, and the kinetic energy E, together with the corresponding power spectra, for M3 at $\mathscr{A} = 79.6$ and $Re = 248.5$.

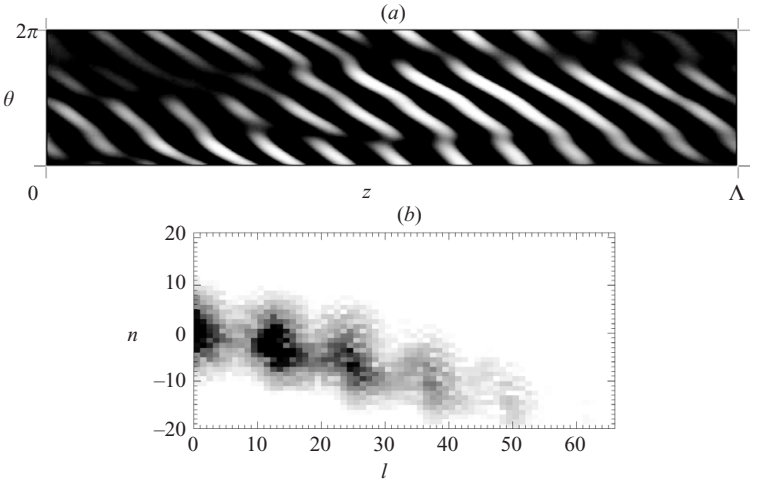

FIGURE 13. (*a*) Planar (z, θ) rendering of a grey-scale map of the azimuthal vorticity of the perturbation $\boldsymbol{u}$ at the outer cylinder $r = r_o$. The flow is M4 at $\mathscr{A} = 79$ and $Re = 250$ (the temporal behaviour is shown in Movie 7 with the online version of the paper). In (*b*) the kinetic energy of the Fourier modes of this state is shown in a logarithmic grey-scale map.

We note that in order to detect this bifurcation, occurring only 1.8% above the first onset of instability, spectral computations considering a small fundamental axial wavenumber k_0, as in the present work, are required. To the authors' knowledge, this is the first time that such an approach has been used in the Taylor–Couette problem.

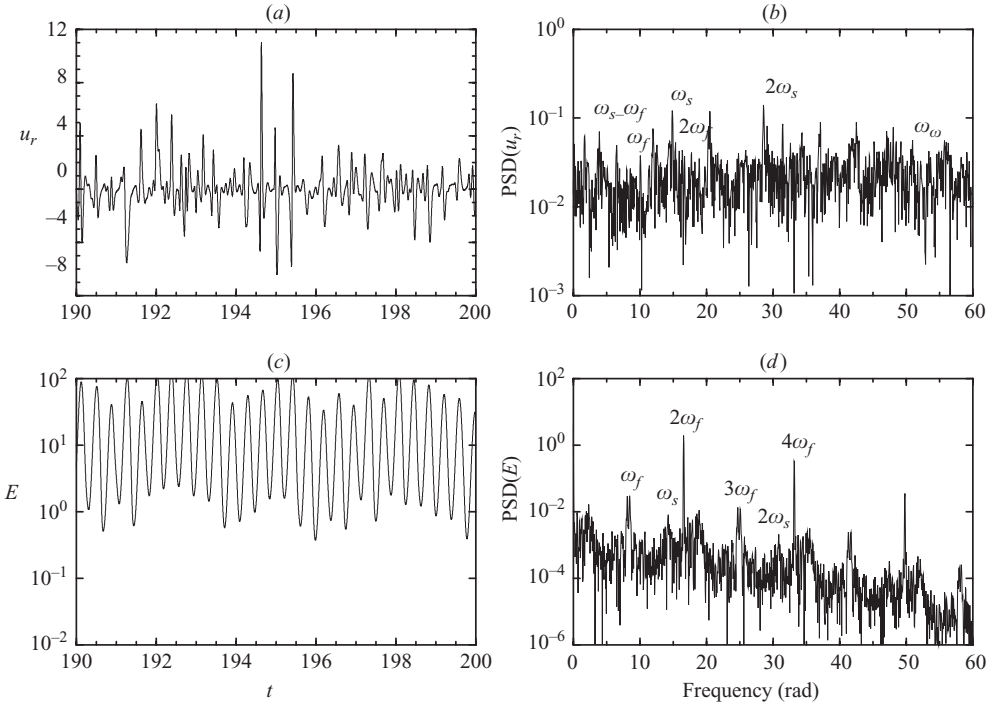

FIGURE 14. Time series of the radial velocity u_r at $(r, \theta, z) = ((r_i + r_o)/2, 0, 0)$, and the kinetic energy E, together with the corresponding power spectra, for M4 in figure 13.

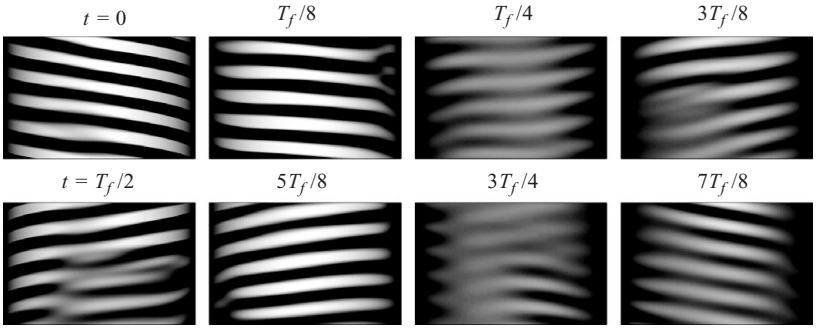

FIGURE 15. A figure 7 but the flow corresponds to M4 at $\mathscr{A} = 79$ and $Re = 250$ shown at 8 phases over one forcing period (temporal behaviour is shown in Movie 8 with the online version of the paper).

In previous works, the fundamental axial wavenumber was set to $k_0 = k_c$, so that defects in the axial wavenumber were not observable due to the imposed periodicity. The flow snapshots of figure 15 (and the temporal behaviour in Movie 8 with the online version) have been computed at $\mathscr{A} = 79$ and $Re = 250$, the same point in parameter space as in figure 8 of Sinha *et al.* (2006). Although these parameter values correspond to the lowest postcritical value of their published data, Re is already 2.4% above the first onset of instability. As the bifurcation from M3 to the non-symmetric M4 occurs before this (1.8% above Re_c), we can conclude that M4 corresponds to the wavy spiral states that are observed in the experiments just following onset. As

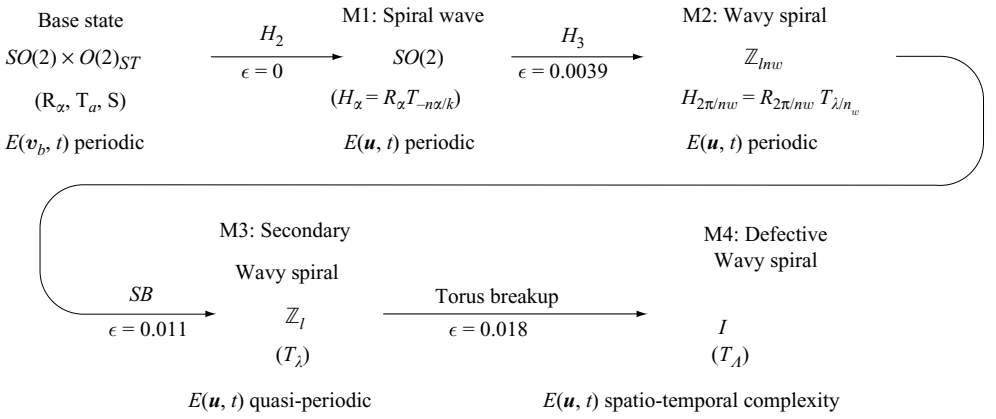

FIGURE 16. Diagram showing the successive bifurcations from the base state to M4 defective wavy spirals. For each solution the symmetry group, its generators and the form of $E(t)$ is indicated. H_n is a Hopf bifurcation to an n-dimensional torus (a relative periodic orbit), and SB is a symmetry-breaking bifurcation of a three torus; the $\epsilon = (Re - Re_c)/Re_c$ at which each of these bifurcations takes place are also indicated ($Re_c = 245.42$).

noted in Sinha *et al.* (2006), the pattern loses spatial regularity very fast, becoming chaotic for higher Re. At this point, the spectral resolution demanded by these states renders our computations impractical, and so we do not pursue them further.

Figure 16 is a schematic of the various solutions obtained, and the bifurcations between them. The starting point is the base state, which is invariant under the full symmetry group of the problem, $\mathcal{G} = SO(2) \times O(2)_{ST}$, leaving the governing equations invariant. Below each stable solution found is the symmetry subgroup leaving the solution invariant, its generators, and the temporal character of the corresponding kinetic energy. The arrows correspond to the different bifurcations we have found in the present study, and each arrow is labelled with the type of bifurcation involved. This sequence of symmetry-breaking bifurcations occurs over about a 2% variation in Re (between about $Re = 245$ and 250), which is about 2/3 of the experimental uncertainty in Re. Figure 17 shows the loci of computed solutions, where the subsequent bifurcations from the basic flow leading to the defective wavy spirals observed in the experiments are detailed in the parameter space.

4. Periodic flow and partial frequency-locking

In the previous section we have described the transition scenario that leads from the simple time-periodic oscillating flow to complex dynamics following several symmetry-breaking bifurcations. When the oscillating basic flow (a periodic orbit) is destabilized via a Neimark–Sacker bifurcation, the flow becomes quasi-periodic, except for the cases where the bifurcating spiral frequency ω_s is resonant with the forcing frequency ω_f, i.e. the rotation number is rational $\omega_s/\omega_f \in \mathbb{Q}$, and then the flow remains periodic. In generic systems, nonlinear behaviour in the neighbourhood of such resonances typically manifests frequency-locking, i.e. there are regions of parameter space where the solution trajectory corresponds to a closed orbit on a two-torus. These regions of frequency-locking typically are shaped like a horn whose tip is a cusp point on the bifurcation curve at which the rotation number is rational (Arnold *et al.* 1999). However, the normal-form analysis presented in Appendix A shows that due to the symmetries of the problem, the dynamics of the bifurcated M1 spiral waves are the same

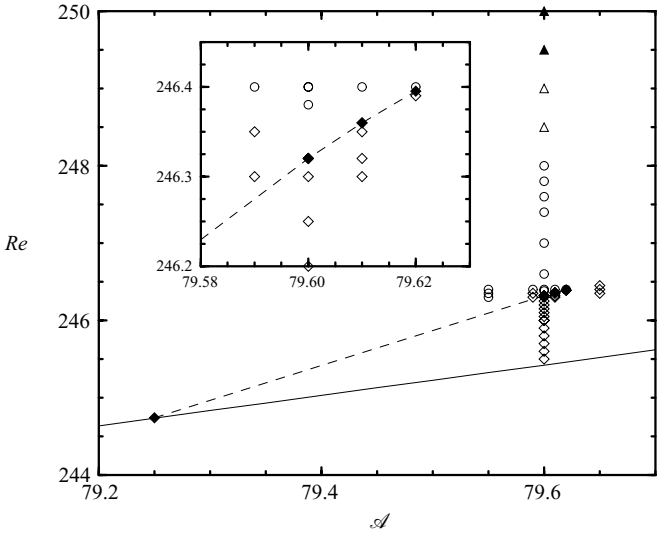

FIGURE 17. Loci of computed solutions for $\eta = 0.905$ and $\omega_f = \mathscr{A}/9.525$, as in Sinha *et al.* (2006). Above the solid line $Re = Re_c(\mathscr{A})$ the basic flow is unstable and evolves to an M1 spiral wave (◇), and to M2 wavy spirals (○) and M3 secondary wavy spirals (△) for higher values of Re. The ▲ indicate M4 defective wavy spirals. The dashed line is the resonance 7/4 curve originating at $\mathscr{A}/9.525 = 79.25$, $Re = 244.74$, and ◆ are M1 on the resonance line.

regardless of whether ω_s/ω_f is rational or irrational. There is no distinction between strong resonances, weak resonances ($\omega_s/\omega_f = \ell/m$, with $m > 4$), or no resonances ($\omega_s/\omega_f \notin \mathbb{Q}$). Therefore, the resonance horns collapse to one-dimensional resonance curves. This is a consequence of the rotational and translational symmetries of the system. Moreover, Appendix B shows that due to the helical symmetry of M1, frequency-locking is also absent following the secondary bifurcation to M2.

In order to detect resonances, we strobe the phase trajectory once every forcing period to produce accurate global Poincaré maps. If the points on the map lie in a set of q clusters then the flow is periodic, whereas a densely filled orbit indicates that the flow is quasi-periodic. Figure 18(a) shows the Poincaré map for an M1 spiral wave at $\mathscr{A} = 79.6$ and $Re = 246.32$ using the phase trajectory given by the axial and azimuthal components of the perturbation $(u_z(t), u_\theta(t))$ recorded at $(r, \theta, z) = ((r_i + r_o)/2, 0, 0)$. Four clusters can be clearly observed. Since $\omega_f = 79.6/9.525 = 8.357$ and the computed value of the spiral frequency at criticality is $\omega_s = 14.61$, then the spiral wave is very close to the $\omega_s/\omega_f = 7/4$ resonance. The presence of a high peak at $\omega = 14.62$ in the power spectra of figure 5(b) together with the four distinct clusters of iterations in the Poincaré map (the close-up of one cluster shows that the iterates are slightly displaced) confirms this hypothesis. When Re is slightly increased by 0.03 to 246.35, the Poincaré map shown in figure 18(b) is very similar, with the small shifts in the iterates of the four clusters more pronounced. We have varied Re in very small increments about this region of parameter space and found no evidence of frequency-locking, in agreement with the equivariant theory in Appendix A. The flow is quasi-periodic and very close to the 7/4 resonance curve (the dashed line in figure 17).

In the previous section it was shown that due to uncertainty in the experiments (about 3% in Re), the states observed in the experiments are in the regime where the flow has no symmetries left. For these M4 states, there is no symmetry restriction on the development of resonance horns, but now the frequency-locking within these

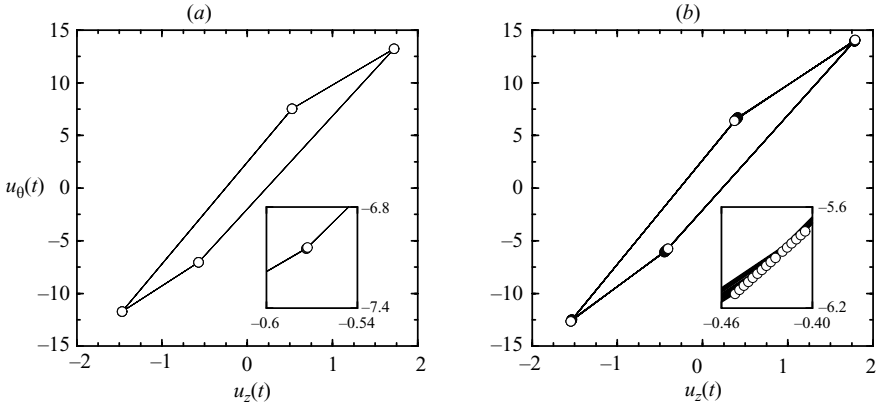

FIGURE 18. Poincaré maps for two M1 solutions, computed with the axial and azimuthal components of the perturbation at $(r, \theta, z) = ((r_i + r_o)/2, 0, 0)$ over several forcing cycles. In (a) the solution is very close to the 7/4 resonance at $\mathscr{A} = 79.6$ and $Re = 246.32$, whereas in (b) at $\mathscr{A} = 79.6$ and $Re = 246.35$, the flow is quasi-periodic, as is indicated by the slight shifts in subsequent iterates of the map in the inset close-up (both close-ups are at the same scale).

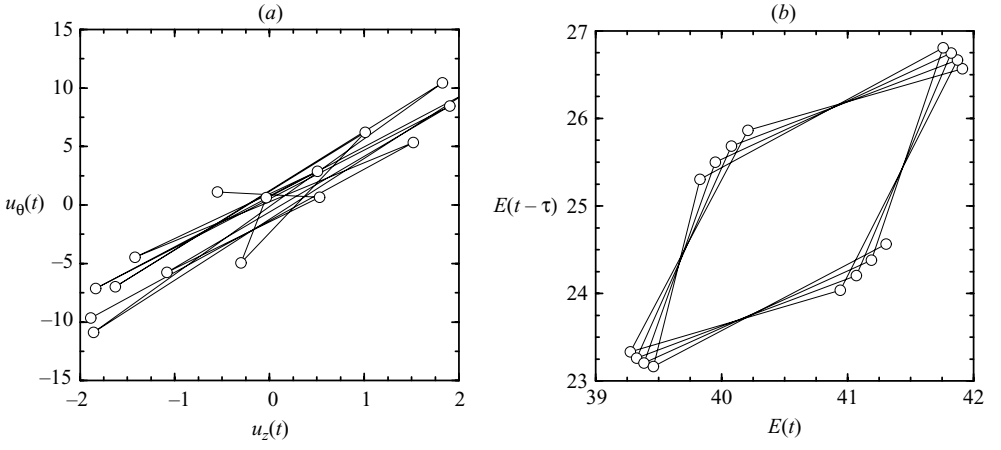

FIGURE 19. Poincaré maps for a secondary wavy spiral M3 at $\mathscr{A} = 79.6$ and $Re = 248.5$ over several forcing cycles. In (a) the axial and azimuthal components of the perturbation at $(r, \theta, z) = ((r_i + r_o)/2, 0, 0)$ are used for the phase trajectory, whereas in (b) the kinetic energy of the perturbation $E(t)$ and the delayed signal $E(t - \tau)$. The time delay is $\tau = 0.452$.

horns must be partial, i.e. only between two of the multiple frequencies that such a complex flow possesses. Figure 19 shows the Poincaré map for secondary wavy spirals M3 at $\mathscr{A} = 79.6$ and $Re = 248.5$ computed from both the azimuthal and axial components of the perturbation and the kinetic energy time series. Due to the multiple independent frequencies that this flow possesses (ω_f, ω_s, ω_w), and the irregularities due to defects in azimuthal wavenumber, there is no identifiable structure in the Poincaré map produced using the velocity. However, the Poincaré map based on the kinetic energy indicates that the solution is close to the 7/4 partial-locking horn. In this case, the kinetic energy acts as a natural filter for some of the frequencies in the flow, in particular those due to the kinematic frequencies associated with the rotation and axial translation of the spiral pattern. In fact, figure 19(b) is similar to the frequency-locking

plots reported in the experiments of Sinha *et al.* (2006). This sheds some light on the apparent discrepancy between the frequency-locking observations reported in these experiments and our theoretical analysis which shows that the symmetries of the basic flow and M1 inhibit frequency-locking. The sequence of symmetry-breaking bifurcations over a very small range in Re removes this restriction and the partial locking is then observable in our nonlinear computations as it is in the experiments.

5. Discussion and conclusions

Nonlinear dynamics of an axially forced Taylor–Couette system has been investigated numerically by solving the unsteady three-dimensional Navier–Stokes equations. In earlier studies, it was shown experimentally (Weisberg *et al.* 1997) and numerically with Floquet analysis of the basic flow (Marques & Lopez 1997) that a high degree of stabilization could be achieved for low frequencies and large amplitudes of the forcing. More recently, the nonlinear dynamics beyond onset of instability was experimentally investigated (Sinha *et al.* 2006), focusing on regions of parameter space where transition is to a spiral mode following a Neimark–Sacker bifurcation.

Our nonlinear numerical explorations have been focused on the same parameter regime as in the experiments by Sinha *et al.* (2006). The flows they observed appeared to contain a high degree of noise, i.e. the signals contained a number of frequencies that could not be identified. Here, using precise spectral computations, we have shown that this apparent noise is due to a sequence of symmetry-breaking bifurcations occurring very close to the primary onset of instability introducing additional independent frequencies. For Re only 0.39% above critical, a secondary bifurcation renders the spiral mode a wavy spiral mode and introduces a third independent frequency. For slightly higher Re, the wavy spirals develop defects in the azimuthal and axial wavenumbers, resulting in spatial and temporal broadband spectra; this is commonly referred to as the onset of soft turbulence. Overall, for Re just 2% above the instability threshold for the basic state, the flow is spatio-temporally very complex. The fine discretization in wavenumber used in the nonlinear computations, combined with careful consideration of the symmetries of the bifurcated flows, is essential to understand the sequence of symmetry-breaking bifurcations that leads from a simple symmetric flow to a very complex pattern.

The experiments showed bands of frequency-locking between the frequency of the forcing and the spiral frequency stemming from the Neimark–Sacker bifurcation. Our theoretical work shows that frequency-locking leading to periodic flow is not possible in the system under consideration. The rotational and translational $SO(2)$ symmetries of the oscillating basic flow annihilate the resonant terms in the normal form of the Neimark–Sacker bifurcation, rendering the dynamics independent of the ratio between frequencies and preventing the formation of resonance horns. However, once the continuous $SO(2)$ symmetries are broken, frequency-locking is permitted. Since there are more than two independent frequencies in this parameter regime, a one-parameter variation will generically only detect regions of partial frequency-locking between two of the frequencies. This partial frequency-locking is very likely the phenomena observed in the experiments, since in the regimes where locking was detected the flow is extremely complex featuring various frequencies and defects in the axial and azimuthal periodicity. Moreover, these additional frequencies account for the noisy Poincaré maps which were used experimentally to identify the regions of locking. This highlights the care that needs to be taken in distinguishing between

extraneous noise and the effects of deterministic bifurcations in accounting for spatio-temporal complex dynamics.

This work was supported by the National Science Foundation grant DMS-05052705, the Spanish Ministry of Education and Science grants FIS2004-01336 and AP-2004-2235, and Catalonian Government grant SGR-00024. Part of the work was done during M. Avila's visit to the Department of Mathematics and Statistics, Arizona State University, whose kind hospitality is warmly appreciated.

Appendix A. Neimark–Sacker bifurcation with $SO(2) \times O(2)_{ST}$ symmetry

The analysis of the dynamics in a neighbourhood of a periodic orbit in a continuous system is greatly simplified by the introduction of the Poincaré map. Generically, the Poincaré map is defined locally, in a neighbourhood of the periodic orbit considered. However, in periodically forced systems like the present problem, there exists a global Poincaré map P, consisting of strobing the flow once every forcing period T_f. The base state, which is synchronous with the forcing, is a T_f-periodic orbit γ that becomes a fixed point of the discrete dynamical system P. The dynamics in a neighbourhood of γ is completely determined once the normal form of the Poincaré map is known. The normal form is a low-dimensional low-order polynomial dynamical system, which is easy to obtain once the critical eigenvectors of γ and their symmetries are known. The critical eigenvectors span a low-dimensional linear subspace tangent to the centre manifold. The amplitudes of these eigenvectors are the natural coordinates of the centre manifold. In our problem, the base state γ depends only on (r, t) and the critical eigenvectors can be Fourier expanded in (θ, z). They are of the form $\boldsymbol{u}_1(r, t)\mathrm{e}^{\mathrm{i}(kz+n\theta)}$, $\boldsymbol{u}_2(r, t)\mathrm{e}^{\mathrm{i}(kz-n\theta)}$, with $n = 1$, and their complex conjugates. The first is a left-handed spiral and the second is a right-handed spiral (both are rotating waves in θ and travelling waves in z). Figure 6 shows the geometrical shapes of these spirals. The centre manifold is four-dimensional, and we use as coordinates the complex amplitudes $(A, B, \bar{A}, \bar{B})$ of the eigenvectors. The four eigenvectors bifurcate simultaneously because the space–time symmetry transforms A into B.

A.1. *Spatial symmetries: generic dynamics*

Let $x \to P(x) = L_P x + N_P(x)$ be the discrete dynamical system considered (the Poincaré map), restricted to the centre manifold, with a fixed point that we assume to be the origin (after a convenient translation if necessary). The map is written as the sum of a linear part, L_P, and a nonlinear part, N_P. The eigenvalues of L_P are the critical eigenvalues, of modulus one. The symmetries of the original problem act on the amplitudes as a linear representation of the symmetry group of the problem, that commute with L_P. However, this applies only to purely spatial symmetries; space–time symmetries require a different treatment.

The normal form of the map, when the symmetries are purely spatial and do not involve time, satisfy the equations (Iooss & Adelmeyer 1998)

$$N_P\left(L_P^\dagger x\right) = L_P^\dagger N_P(x), \qquad N_P(Gx) = GN_P(x), \ \forall G \in \mathscr{G}_0, \tag{A 1}$$

where $L_P^\dagger$ is the adjoint (conjugated and transposed) of L_P. The symmetry group of the spatial symmetries of the system under consideration is $\mathscr{G}_0 = SO(2) \times SO(2)$ and it is generated by rotations R_α about, and translations T_a along, the common axis of the cylinders. The actions of R_α and T_a on the amplitudes $x = (A, B, \bar{A}, \bar{B})$ are

$$R_\alpha = \mathrm{diag}(\mathrm{e}^{\mathrm{i}n\alpha}, \mathrm{e}^{-\mathrm{i}n\alpha}, \mathrm{e}^{-\mathrm{i}n\alpha}, \mathrm{e}^{\mathrm{i}n\alpha}), \quad T_a = \mathrm{diag}(\mathrm{e}^{\mathrm{i}ka}, \mathrm{e}^{\mathrm{i}ka}, \mathrm{e}^{-\mathrm{i}ka}, \mathrm{e}^{-\mathrm{i}ka}). \tag{A 2}$$

As L_P commutes with R_α and T_a, it must be diagonal. Let $e^{i\beta_1}$ be the eigenvalue corresponding to A. As the space–time symmetry S transforms A into B, both have the same eigenvalue. Therefore, L_P must be of the form

$$L_P = \mathrm{diag}(e^{i\beta_1}, e^{i\beta_1}, e^{-i\beta_1}, e^{-i\beta_1}), \tag{A 3}$$

where β_1 is related to the spiral frequency ω_s as $\beta_1 = \omega_s T_f = 2\pi\,\omega_s/\omega_f$. The normal form for the Poincaré map is

$$P : \begin{cases} A \to e^{i\beta_1} A + N_1(A, B, \bar{A}, \bar{B}), \\ B \to e^{i\beta_1} B + N_2(A, B, \bar{A}, \bar{B}), \end{cases} \tag{A 4}$$

plus complex conjugates. Let $A^p B^q \bar{A}^r \bar{B}^j$ be a monomial in N_1. The first equation in (A 1) is a particular case of the second, because L_P coincides with an axial translation $a = \beta_1/k$ ($L_P = T_{\beta_1/k}$). The second equation in (A 1) results in

$$\left.\begin{aligned} e^{in\alpha(p-q-r+j)} &= e^{in\alpha} \\ e^{ika(p+q-r-j)} &= e^{ika} \end{aligned}\right\} \;\Rightarrow\; \left.\begin{aligned} p-q-r+j &= 1 \\ p+q-r-j &= 1 \end{aligned}\right\} \;\Rightarrow\; p = r+1,\ q = j, \tag{A 5}$$

so $N_1(A, B, \bar{A}, \bar{B}) = A\,Q_1(|A|^2, |B|^2)$, and analogously for N_2. Equation (A 4) reduces to

$$P : \begin{cases} A \to e^{i\beta_1} A(1 + Q_1(|A|^2, |B|^2)), \\ B \to e^{i\beta_1} B(1 + Q_2(|A|^2, |B|^2)), \end{cases} \tag{A 6}$$

where a factor $e^{-i\beta_1}$ has been included in Q_i for convenience. Some important consequences of this normal form are worth noting. First, there are no resonant terms, therefore the normal form is the same regardless of whether $\beta_1/2\pi$ is rational or irrational. In particular, there is no distinction between strong resonances ($\beta_1/2\pi = \ell/m$, with $m = 1$, 2, 3 or 4), weak resonances ($m > 4$), or no resonances at all ($\beta_1/2\pi \notin \mathbb{Q}$). This is a consequence of the rotational and translational symmetry of the system, i.e. the spatial symmetry group $\mathcal{G}_0 = SO(2) \times SO(2)$. Another important consequence is the absence of frequency-locking phenomena. Generically, frequency-locking takes place when resonant terms (different from $A|A|^2$ and $A|B|^2$ in N_1, and analogously in N_2) couple the modulus and phase dynamics of A and B. By introducing $A = r_1 e^{i\phi_1}$ and $B = r_2 e^{i\phi_2}$, the normal form (A 6) can be written as

$$P : \begin{cases} r_1 \to r_1\big(1 + Q_{1,1}\big(r_1^2, r_2^2\big)\big), \\ r_2 \to r_2\big(1 + Q_{2,2}\big(r_1^2, r_2^2\big)\big), \end{cases} \quad \begin{cases} \phi_1 \to \phi_1 + \beta_1 + Q_{1,2}\big(r_1^2, r_2^2\big), \\ \phi_2 \to \phi_2 + \beta_1 + Q_{2,1}\big(r_1^2, r_2^2\big), \end{cases} \tag{A 7}$$

and the modulus dynamics (r_1 and r_2) decouples from the phase dynamics (ϕ_1 and ϕ_2). The decoupling is the cause of the suppression of the frequency-locking phenomena.

This frequency-locking suppression is very similar to the result of Rand (1982, Theorem 3 and Remark) that Hopf bifurcations from rotating waves do not manifest frequency-locking, due to the rotational symmetry. In our case, the base state is not a rotating wave, but it is independent of the azimuthal and axial coordinates, i.e. it is a $SO(2) \times SO(2)$ symmetric periodic orbit. The breaking of these symmetries results in modulated spiral waves that do not manifest frequency-locking. There has been a great deal of work concerning bifurcations from periodic orbits generalizing Rand's original work (Krupa 1990; Lamb, Melbourne & Wulff 2003), from which our result, complementary to Rand's, can be obtained. We have kept the result in the Appendix for completeness.

A.2. *Space–time symmetry S*

Now consider the implications of the space–time symmetry S. The square of S is the identity on the base state of the system, but acting on an arbitrary solution results in the global Poincaré map P: the two axial reflections F_z cancel each other, and the total advance in time is the period of the forcing T_f. The fact that the Poincaré map is a square, $P = S^2$, has important implications for the dynamics (see for example Swift & Wiesenfeld 1984, when the critical eigenvalues are simple). A powerful and simple way to take into account the space–time symmetry is to analyse the normal form of S and recover the Poincaré map normal form by squaring it. This has been done, for example, in Marques, Lopez & Blackburn (2004) for a system with spatial symmetry $O(2)$ and spatio-temporal symmetry Z_2. The analysis in that case was facilitated by the fact that the spatio-temporal symmetry commuted with the spatial symmetries, and the conditions to be satisfied by the normal form of S were the same as in (A 1), just replacing L_P by L_S. But in the present problem, S does not commute with the axial translations T_a (in fact $ST_a = T_{-a}S$), so we need to establish what are the conditions to be satisfied by the normal form of S. The condition $N(Gx) = GN(x)$ must be changed to a more general condition that includes the case of non-commutativity of the spatial symmetries with S, and in particular with their linear part L_S. The discrete dynamical system S is a map $S : x \to F(x)$, but now F is not $\mathscr{G}_0$-equivariant (i.e. $F(Gx) \neq GF(x)$, $\forall G \in \mathscr{G}_0$). This is because there exist elements of $\mathscr{G}_0$ that do not commute with S (e.g. the axial translations T_a). Inspired by, and following the work of Lamb & Melbourne (1999) (and references therein), we say that F satisfies a *twisted equivariance condition* of the form

$$F(Gx) = \psi(G)F(x), \quad \forall G \in \mathscr{G}_0, \tag{A 8}$$

where ψ is an automorphism of $\mathscr{G}_0$. This automorphism is fixed by the same twisted equivariance condition on the linear part of S, $L_S(Gx) = \psi(G)L_S(x)$, i.e. $\psi(G) = L_S G L_S^{-1}$. Summarizing, if the normal form of S is $x \to S(x) = L_S x + N(x)$, the conditions on N are of the form

$$N\left(L_S^{\dagger}x\right) = L_S^{\dagger}N(x), \;\; N(Gx) = \psi(G)N(x), \;\; \forall G \in \mathscr{G}_0, \;\; \text{where } \psi(G) = L_S G L_S^{-1}. \tag{A 9}$$

Notice that when L_S commutes with $\mathscr{G}$ (as in Marques *et al.* 2004), the inner automorphism becomes the identity, and we recover the ordinary equivariant condition (A 1). What is the action of L_S on the centre manifold? The centre manifolds and eigenvectors of P and their square-root S are the same, and the eigenvalues of P are the eigenvalues of S squared. However, there is some freedom in the form of L_S, because the eigenvalues are of multiplicity two (e.g. the two-dimensional eigenspace associated with the eigenvalue $\mathrm{e}^{\mathrm{i}\beta_1}$ has A and B as coordinates). This freedom is fixed since L_S must transform A into B, because the axial reflection F_z transforms the left-handed spiral A into the right-handed spiral B (modulus the time translation $T/2$). The action of L_S on the complex amplitudes $(A, B, \bar{A}, \bar{B})$ is

$$L_S = \begin{pmatrix} 0 & \mathrm{e}^{\mathrm{i}\beta_1/2} & 0 & 0 \\ \mathrm{e}^{\mathrm{i}\beta_1/2} & 0 & 0 & 0 \\ 0 & 0 & 0 & \mathrm{e}^{-\mathrm{i}\beta_1/2} \\ 0 & 0 & \mathrm{e}^{-\mathrm{i}\beta_1/2} & 0 \end{pmatrix} \tag{A 10}$$

and the actions of R_α and T_a are unchanged, given by (A 2). The automorphism ψ can be explicitly computed: $\psi(R_\alpha) = R_\alpha$, $\psi(T_a) = T_{-a}$, reflecting the fact that S commutes with R_α, but $ST_a = T_{-a}S$; ψ is an involution, $\psi^2 = Id$, reflecting the fact

that $S^2 = P$. Having explicitly obtained the actions of L_S, ψ and $\mathscr{G}_0$, we can work out the conditions (A 9). The normal form for the space–time map S is of the form

$$S : \begin{cases} A \to e^{i\beta_1/2} B + N_3(A, B, \bar{A}, \bar{B}), \\ B \to e^{i\beta_1/2} A + N_4(A, B, \bar{A}, \bar{B}). \end{cases} \tag{A 11}$$

Let $A^p B^q \bar{A}^r \bar{B}^j$ be a monomial in N_3. Following the same lines as in the purely spatial symmetries case, we obtain

$$S : \begin{cases} A \to e^{i\beta_1/2} B(1 + Q(|B|^2, |A|^2)), \\ B \to e^{i\beta_1/2} A(1 + Q(|A|^2, |B|^2)). \end{cases} \tag{A 12}$$

Instead of two arbitrary functions Q_3 and Q_4, there is only one, Q, because L_S transforms A into B. By squaring the map, the normal form of the Poincaré map P (A 6) is obtained, but thanks to the use of the space–time symmetry S, we obtain

$$Q_1(|A|^2, |B|^2) = Q_2(|B|^2, |A|^2) = \tilde{Q}(|A|^2, |B|^2), \tag{A 13}$$

where $\tilde{Q}$ is a complex-coefficient polynomial; this is the constraint imposed by the space–time symmetry S on the normal form of the Poincaré map. The relationship between Q and $\tilde{Q}$ is easy to obtain, but convoluted†. In terms of the moduli and phases of A and B, the normal form of the Poincaré map (A 7) reduces to

$$P : \begin{cases} r_1 \to r_1\big(1 + Q_m\big(r_1^2, r_2^2\big)\big), \\ r_2 \to r_2\big(1 + Q_m\big(r_2^2, r_1^2\big)\big), \end{cases} \quad \begin{cases} \phi_1 \to \phi_1 + \beta_1 + Q_p\big(r_1^2, r_2^2\big), \\ \phi_2 \to \phi_2 + \beta_1 + Q_p\big(r_2^2, r_1^2\big), \end{cases} \tag{A 14}$$

where the polynomials Q_m and Q_p have real coefficients: $1 + \tilde{Q} = (1 + Q_m)\exp(iQ_p)$. The moduli dynamics decouples from the phase dynamics, and we end up with a two-dimensional reduced normal form, the first two equations in (A 14). As the polynomial Q_m is the same in r_1 and r_2, the fixed points of the reduced normal form are of the form (r, r), including $(0, 0)$ which is the base state, or they come in symmetric pairs (r, r') and (r', r). In the complete problem, the fixed points of the form $(0, r)$, $(r, 0)$ and (r, r), $r \neq 0$, are quasi-periodic solutions with two frequencies, and the fixed points of the form (r, r'), $r \neq r' \neq 0$, correspond to three-frequency solutions.

A.3. *Bifurcation scenarios*

In order to explore the dynamics in a neighbourhood of the bifurcation, the normal form for S (A 12) is truncated up to fourth-order terms, and written in terms of the moduli and phases of A and B:

$$S : \begin{cases} r_1 \to r_2\big(1 + \mu - a r_2^2 - b r_1^2\big), \\ r_2 \to r_1\big(1 + \mu - a r_1^2 - b r_2^2\big), \end{cases} \quad \begin{cases} \phi_1 \to \phi_2 + \beta_1/2 + \nu + c r_2^2 + d r_1^2, \\ \phi_2 \to \phi_1 + \beta_1/2 + \nu + c r_1^2 + d r_2^2. \end{cases} \tag{A 15}$$

Note that the symmetry group of this normal form is $Z_2 \times Z_2$. One of the symmetries corresponds to the exchange between r_1 and r_2 ($r_1 \leftrightarrow r_2$), and comes from the space–time symmetry S. The other Z_2 symmetry ($r \leftrightarrow -r$) comes from the use of polar coordinates. The bifurcation is of codimension two (two independent parameters μ and ν), but the reduced system is of codimension one since the parameter ν only affects the phase dynamics. The only fixed points of the reduced planar system (r_1, r_2)

† The precise expression is $\tilde{Q}(x, y) = \{1 + Q(x, y)\}\{1 + Q(x|1 + Q(x, y)|^2, y|1 + Q(y, x)|^2)\} - 1$.

in a neighbourhood of the origin are of the form (r, r), and there are two of them:

$$p_0 = (0, 0), \quad p_3 = \Big(\sqrt{\frac{\mu}{a+b}}, \sqrt{\frac{\mu}{a+b}}\Big). \tag{A 16}$$

The corresponding eigenvalues (in the reduced system for S) are

$$p_0: \quad \lambda_1 = 1+\mu, \quad \lambda_2 = -1-\mu, \tag{A 17}$$

$$p_3: \quad \lambda_1 = 1-2\mu, \quad \lambda_2 = -1+2\,\frac{a-b}{a+b}\,\mu. \tag{A 18}$$

The eigenvalues of the corresponding reduced system for P are the same squared. The base state is p_0, it exists for any μ value, it is stable for $\mu<0$ and unstable for $\mu>0$; p_3 exists only for $\mu/(a+b)>0$, and is stable for $a-b>0$ and $\mu>0$. Both p_0 and p_3 are invariant under the space–time symmetry S. The bifurcation is supercritical for $a+b>0$ and subcritical for $a+b<0$. The bifurcated state p_3 is a linear combination with the same weight ($|A|=|B|$) of the left-handed and right-handed spirals, which travel in opposite axial directions; p_3 therefore corresponds to a modulated standing wave, MSW.

We can also look for periodic orbits of S, of period two, and these are fixed points of the Poincaré map P. As $P=S^2$, from (A 15) we obtain

$$P: \begin{cases} r_1 \to r_1\big(1+2\mu-2ar_1^2-2br_2^2\big), \\ r_2 \to r_2\big(1+2\mu-2ar_2^2-2br_1^2\big), \end{cases} \quad \begin{cases} \phi_1 \to \phi_1+\beta_1+2\nu+2cr_1^2+2dr_2^2, \\ \phi_2 \to \phi_2+\beta_1+2\nu+2cr_2^2+2dr_1^2. \end{cases} \tag{A 19}$$

The fixed points of the reduced planar system, of the form (r, r), are the same p_0 and p_3 already obtained. But there is a pair of new fixed points of P:

$$p_1 = (\sqrt{\mu/a}, 0), \quad p_2 = (0, \sqrt{\mu/a}), \tag{A 20}$$

that exist for $\mu/a>0$. The fixed points p_1 and p_2 correspond to periodic orbits of period two of the space–time symmetry S that transforms one into the other: $Sp_1=p_2$, $Sp_2=p_1$, as can be checked directly in (A 15). Here p_1 is a left-handed spiral, a travelling wave in the axial direction; p_2 is a right-handed spiral, traversing in the opposite axial direction. Both are modulated travelling wave solutions, MTW, that break the space–time symmetry. They have the same eigenvalues (in the reduced system for P), which are

$$p_1,\ p_2: \quad \lambda_1 = 1-4\mu, \quad \lambda_2 = 1+2\frac{a-b}{a}\mu, \tag{A 21}$$

and they are stable if $\mu>0$ and $a<b$.

When $a=0$ or $a+b=0$ or $a-b=0$, there are degeneracies between the fixed points p_i and/or their eigenvalues, so we will assume $a\neq 0$ and $a+b\neq 0$ and $a-b\neq 0$. The bifurcation has six different scenarios, corresponding to the six regions in parameter space delimited by the curves $a=0$, $a+b=0$ and $a-b=0$, as illustrated in figure 20. The phase portraits for the six scenarios are schematically drawn in figure 21. The scenarios and phase portraits in figures 20 and 21 occur in a number of contexts involving symmetry-breaking Hopf bifurcations (see Crawford & Knobloch 1991, and references therein). As the bifurcation is of codimension one and takes place for $\mu=0$, we have plotted the phase portraits for the reduced system (r_1, r_2) before and after the bifurcation.

In the first (I) and second (II) scenarios, the two modulated travelling waves and the modulated standing wave bifurcate simultaneously and supercritically from the

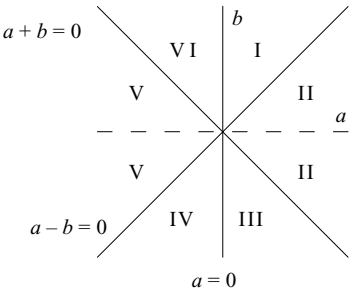

FIGURE 20. Regions in parameter space where different dynamics exist. The corresponding phase portraits are shown in figure 21.

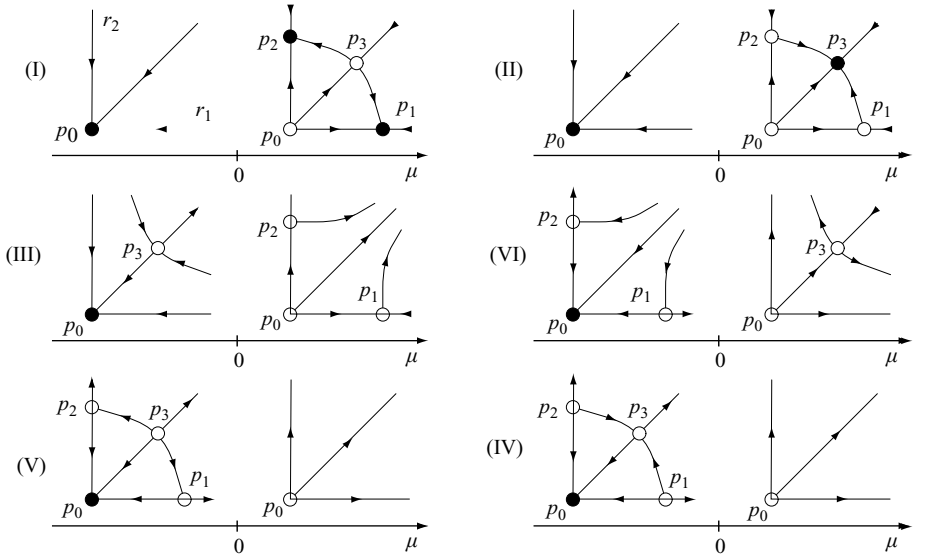

FIGURE 21. Phase portraits corresponding to the six bifurcation scenarios in figure 20. Phase portraits for the reduced system (r_1, r_2) have been plotted before $(\mu < 0)$ and after $(\mu > 0)$ the bifurcation.

base state, that becomes unstable. In the first scenario the MTW are stable and the MSW is unstable. In the second scenario it is the opposite. In the (IV) and (V) scenarios, the two modulated travelling waves and the modulated standing wave bifurcate simultaneously and subcritically from the base state, that becomes unstable. The travelling and standing waves are always unstable, so after the bifurcation ($\mu > 0$) there are no stable solutions close to the origin, and the system evolves far away from the base state. The only difference between the two scenarios is in the number of unstable directions of the standing wave, one and two in scenarios (IV) and (V) respectively. In the (III) scenario, the base state becomes unstable by colliding with the unstable MSW, and after the bifurcation the two MTW emerge but are unstable, and the system evolves far away from the base state, as there are no stable states close to the origin. Finally, in the (VI) scenario, the base state becomes unstable by colliding with the two unstable MTW, and after the bifurcation the MSW emerge but are unstable, and the system evolves far away from the base state as before. In

the system under consideration, and for the parameter values analysed, the second scenario (II) takes place.

Appendix B. Neimark–Sacker bifurcation with $SO(2)$ symmetry

The M1 spiral waves perturbation velocity field depends on (θ, z) only in the combination $\omega_s t + kz + n\theta$. After the bifurcation, an additional dependence on $\omega_w t + n_w \theta$ appears, therefore the critical eigenvector is of the form $\boldsymbol{f}(r, t, \omega_s t + kz + n\theta)\mathrm{e}^{\mathrm{i}(\omega_w t + n_w \theta)}$. In fact we do not have a pair of complex-conjugate eigenvectors, but rather an infinite family. This is because the action of R_α does not leave an M1 spiral wave invariant (the bifurcation to M1 has broken the rotational symmetry), but changes its phase in the azimuthal direction. The Poincaré map (strobing with the forcing period T_f) has a pair of complex-conjugate eigenvectors of modulus one at the bifurcation point, given by $\mathrm{e}^{\pm \mathrm{i}\beta_2}$ with $\beta_2 = \omega_w T_f = 2\pi\, \omega_w/\omega_f$. It also has a centre direction corresponding to the continuous symmetry broken at the bifurcation to M1, so the centre manifold is three-dimensional. Nevertheless, as M1 is a relative periodic orbit, the dynamics in this third direction decouples from the dynamics corresponding to the pair of complex-conjugate eigenvectors (see Wulff *et al.* 2001), so the bifurcation can be analysed as being effectively two-dimensional, spanned by the mentioned eigenvector and its complex conjugate, and can be parameterized by a complex amplitude A. The normal form $x \to P(x) = L_P x + N_P(x)$, with $x = (A, \bar{A})$ must satisfy (A 1), where the symmetry group is now $\mathscr{G}_0 = SO(2)$, generated by the helical motion $H_\alpha = R_\alpha T_{-n\alpha/k}$, and no spatio-temporal symmetries exist. The action of L_P and H_α on $(A, \bar{A})$ is easy to obtain from the (θ, z) dependence of the eigenvectors, and is

$$L_P = \mathrm{diag}(\mathrm{e}^{\mathrm{i}\beta_2}, \mathrm{e}^{-\mathrm{i}\beta_2}), \quad H_\alpha = \mathrm{diag}(\mathrm{e}^{\mathrm{i}n_w\alpha}, \mathrm{e}^{-\mathrm{i}n_w\alpha}). \tag{B 1}$$

$L_P = H_{\beta_2/n_w}$, showing that the bifurcated solution is a modulated spiral wave: advancing a forcing period is equivalent to a helical motion. The conditions (A 1) on the normal form result in $N_P(A, \bar{A}) = A\tilde{Q}(|A|^2)$ and the normal form is

$$P : A \to \mathrm{e}^{\mathrm{i}\beta_2} A(1 + Q(|A|^2)), \tag{B 2}$$

where a factor $\mathrm{e}^{-\mathrm{i}\beta_2}$ has been included in Q for convenience. This is the normal form of a non-resonant Neimark–Sacker bifurcation (Kuznetsov 1998), the absence of resonant terms being due to the presence of the helical symmetry group $SO(2)$, irrespective of $\beta_2/2\pi = \omega_w/\omega_f$ being rational or irrational. The bifurcated solution retains a discrete helical symmetry: from (B 1), $H_{2\pi/n_w}$ is the identity on the bifurcated solutions, and their symmetry group is discrete, $\mathbb{Z}_{ln_w}$, generated by the helical motion $H_{2\pi/n_w}$. Notice that in this bifurcation the axial periodicity is not altered: $H^{n_w}_{2\pi/n_w} = T_\lambda$, an axial translation of the wavelength of the spiral wave.

REFERENCES

Ali, M. E. & Weidman, P. D. 1993 On the linear stability of cellular spiral Couette flow. *Phys. Fluids* A **5**, 1188–1200.

Andereck, C. D., Liu, S. S. & Swinney, H. L. 1986 Flow regimes in a circular Couette system with independently rotating cylinders. *J. Fluid Mech.* **164**, 155–183.

Arnold, V. I., Afrajmovich, V. S., Il'yashenko, Y. S. & Shil'nikov, L. P. 1999 *Bifurcation Theory and Catastrophe Theory*. Springer.

Avila, M., Meseguer, A. & Marques, F. 2006 Double Hopf bifurcation in corotating spiral Poiseuille flow. *Phys. Fluids* **18**, 064101.

Coles, D. 1965 Transition in circular Couette flow. *J. Fluid Mech.* **21**, 385–425.

Crawford, J. D. & Knobloch, E. 1991 Symmetry and symmetry-breaking bifurcations in fluid dynamics. *Annu. Rev. Fluid Mech.* **23**, 341–387.

Hu, H. C. & Kelly, R. E. 1995 Effect of a time-periodic axial shear flow upon the onset of Taylor vortices. *Phys. Rev.* E **51**, 3242–3251.

Iooss, G. & Adelmeyer, M. 1998 *Topics in Bifurcation Theory and Applications*, 2nd edn. Advanced Series in Nonlinear Dynamics, vol. 3. World Scientific.

Jones, C. A. 1985 Numerical methods for the transition to wavy Taylor vortices. *J. Comput. Phys.* **61**, 321–344.

Krupa, M. 1990 Bifurcations of relative equilibria. *SIAM J. Math. Anal.* **21**, 1453–1486.

Kuznetsov, Y. A. 1998 *Elements of Applied Bifurcation Theory*, 2nd edn. Springer.

Lamb, J. S. W. & Melbourne, I. 1999 Bifurcation from discrete rotating waves. *Arch. Rat. Mech. Anal.* **149**, 229–270.

Lamb, J. S. W., Melbourne, I. & Wulff, C. 2003 Bifurcation from periodic solutions with spatiotemporal symmetry, including resonances and mode interactions. *J. Diffl Equat.* **191**, 377–407.

Ludwieg, H. 1964 Experimentelle Nachprufung des stabilitatstheorien fur reibungsfreie Stromungen mit schraubenlinienformigen stromlinien. *Z. Flugwiss* **12**, 304–309.

Lueptow, R. M., Docter, A. & Min, K. 1992 Stability of axial flow in an annulus with a rotating inner cylinder. *Phys. Fluids* A **4**, 2446–2455.

Marques, F. & Lopez, J. M. 1997 Taylor-Couette flow with axial oscillations of the inner cylinder: Floquet analysis of the basic flow. *J. Fluid Mech.* **348**, 153–175.

Marques, F. & Lopez, J. M. 2000 Spatial and temporal resonances in a periodically forced hydrodynamic system. *Physica* D **136**, 340–352.

Marques, F., Lopez, J. M. & Blackburn, H. M. 2004 Bifurcations in systems with Z_2 spatio-temporal and $O(2)$ spatial symmetry. *Physica* D **189**, 247–276.

Meseguer, A. & Marques, F. 2000 On the competition between centrifugal and shear instability in spiral Couette flow. *J. Fluid Mech.* **402**, 33–56.

Meseguer, A. & Marques, F. 2002 On the competition between centrifugal and shear instability in spiral Poiseuille flow. *J. Fluid Mech.* **455**, 129–148.

Rand, D. 1982 Dynamics and symmetry. Predictions for modulated waves in rotating fluids. *Arch. Rat. Mech. Anal.* **79**, 1–37.

Sinha, M., Kevrekidis, I. G. & Smits, A. J. 2006 Experimental study of a Neimark–Sacker bifurcation in axially forced Taylor–Couette flow. *J. Fluid Mech.* **558**, 1–32.

Snyder, H. A. 1962 Experiments on the stability of spiral flow at low axial Reynolds numbers. *Proc. R. Soc. Lond.* A **265**, 198–214.

Swift, J. W. & Wiesenfeld, K. 1984 Suppression of period doubling in symmetric systems. *Phys. Rev. Lett.* **52**, 705–708.

Tagg, R. 1994 The Couette-Taylor problem. *Nonlinear Sci. Today* **4**, 1–25.

Takeuchi, D. I. & Jankowski, D. F. 1981 A numerical and experimental investigation of the stability of spiral Poiseuille flow. *J. Fluid Mech.* **102**, 101–126.

Tsameret, A. & Steinberg, V. 1994 Competing states in a Couette–Taylor system with an axial flow. *Phys. Rev.* E **49**, 4077–4086.

Weisberg, A. Y., Kevrekidis, I. G. & Smits, A. J. 1997 Delaying transition in Taylor–Couette flow with axial motion of the inner cylinder. *J. Fluid Mech.* **348**, 141–151.

Wereley, S. T. & Lueptow, R. M. 1999 Velocity field for Taylor-Couette flow with an axial flow. *Phys. Fluids* **11**, 3637–3649.

Wulff, C., Lamb, J. S. W. & Melbourne, I. 2001 Bifurcation from relative periodic solutions. *Ergod. Theor. Dyna. Sysst.* **21**, 605–635.